Cite this paper: Chang, Z.-W.; Meng, F.-L.; Zhong, H.-X.; Zhang, X.-B. *Chin. J. Chem.* **2018**, *36*, 287—292.

Comprehensive Report

DOI: 10.1002/cjoc.201700752

Anchoring Iron-EDTA Complex on Graphene toward the Synthesis of Highly Efficient Fe-N-C Oxygen Reduction Electrocatalyst for Fuel Cells

Zhi-Wen Chang,[a,b] Fan-Lu Meng,[a] Hai-Xia Zhong,[a] and Xin-Bo Zhang *[,a]

ABSTRACT Developing nonprecious carbon electrocatalysts as alternatives to platinum for cathodic oxygen reduction reaction in fuel cells is of significance. Herein, an efficient precursor-controlled synthesis strategy based on extremely rapid nucleation and deposition process assisted by the liquid nitrogen freeze drying method is explored to anchor cheap iron-EDTA complex evenly dispersed on graphene to realize microstructural homogeneity of the derived Fe-N-C oxygen reduction electrocatalyst. The prepared electrocatalyst possesses excellent performance including high activity with more positive onset and half-wave potential, a long-term stability, and anti-poisoning effect compared to commercial Pt/C. The activity correlates well with the unique sheet-shaped morphology, high surface area, hierarchical porous structure, and the introduction of Fe-Nx/C species. Especially, both the assembled practical alkaline and acid fuel cells based on the synthesized cathode catalysts reveal excellent performance with high open-circuit voltage and power density.

KEYWORDS iron-EDTA complex, iron-nitrogen-doping carbon, porous nanosheets, oxygen reduction reaction, fuel cells

Introduction

Global energy-demand growth and the austere risks of global climate, environment, and social issues caused by the use of traditional energy resources along with economic development, have attracted a lot of researchers' attention upon clean and efficient energy conservation and storage devices. As clean and advanced electrochemical technologies, fuel cells and metal-air batteries can be the best choice.[1-4] In these electrochemical applications, the oxygen reduction reaction (ORR) at cathodes plays a key role, but rather slow ORR kinetics unavoidably cause severe loss of energy efficiency due to the exceptionally high O=O bond energy and multi-electron transfer.[5-8] Platinum (Pt) and/or its alloys are widely referred to as the most efficient ORR electrocatalysts.[9-12] However, until now, their large-scale industrialization and commercial applications have always been limited by several serious problems, including the high cost and scarcity, and technological bottlenecks, such as the poor stability and crossover and poisoning effects.[13-17] Therefore, in order to smooth away all these difficulties, developing alternative low-cost, stable and efficient nonprecious metals catalysts (NPMCs) is thus of great importance.

Quite recently, many kinds of nonprecious metals materials[18-35] including metal-free heteroatom (N, B, S) doped carbons,[18-23] transition metal (Fe, Co)-coordinating N-C (M-N-C) materials,[24-31] and metal oxides[33,34] have been employed as NPMCs. Typically, M-N-C materials are widely supposed to be the most efficient NPMCs for ORR with high expectations. Direct calcining the mixture of single and/or plural precursors of carbon, nitrogen, and transition metal salts is the most common preparation method. However, it is difficult to control the uniform dispersion of different components based on the simple physical mixture of these precursors, which probably results in the uncontrolled agglomeration and microstructural inhomogeneity of M-N-C materials during the pyrolysis process.[36,37] Precursor-controlled synthesis has proven to be a very attractive approach, wherein, precursors with intrinsic metal-nitrogen coordination relationship seem to make the most sense. In particular, (Fe, Co)-based coordination complex, such as metalloporphyrin, metallophthalocyanine and their polymers and the metal organic frameworks (MOFs) are usually applied as the most efficient precursors.[38-40] Despite the achievement of satisfactory activities which are even better than those of the commercial Pt/C catalysts, commonly high prices and/or highly complex synthetic processes will inevitably limit their large-scale practical application. Thus, how to take advantage of the precursor-controlled synthesis to achieve a homogeneous composite system, while limiting costs based on cheap transition metals coordination complex is a challenge and arduous task.

Herein, as a proof of concept, we demonstrate an effective strategy to anchor the cheap iron-EDTA complex on graphene to construct the homogeneous precursor composite, in which, the iron-EDTA complex evenly disperses on graphene oxide (GO) through dissolution, rapid nucleation and deposition process assisted by the liquid nitrogen cooling. The naturally chelate properties of iron-EDTA guarantee homogeneous mixing of the Fe ions in N and C components on atomic scale. Furthermore, the graphenes serve as templates and form two dimensionally (2D) conterminous conductive networks ensuring fast and continuous mass transfer, the evaporation of sodium (Na) and Fe particles both of which act as template roles creates abundant graded pores. Profiting from the synergistic effect of structure and composition, the carbonization derived Fe-N-C catalyst presents advantageous catalytic properties for ORR in alkaline media, including high activity, excellent stability, and anti-poisoning power, all of which are superior to those of commercial Pt/C catalysts. In addition, it can even possess competitive ORR catalytic performance in acid environment, and can be successfully applied to practical proton and alkaline exchange membrane fuel cells as promising cathode catalysts with high open-circuit voltage and peak power capacity.

Results and Discussion

The synthesis procedure of EFGC is exhibited in Figure 1 schematically. In brief, the EDTA-Fe-Na/GO precursor was synthesized through a simple freeze drying method assisted by gelid liquid nitrogen with a high yield, inspired by a natural principle in sea ice.[41] Mechanically, the EDTA-Fe-Na dissolved is banished from the forming ice rapidly under sudden cold conditions along with the dumped liquid nitrogen, therewith goes through quick nucleation and growth along the surface of GO homogenously. Wherein, the GO is wrapped in channels between ice crystals to prevent clumping of GO in the following vacuum drying and ensure that it offers an ultrathin two-dimensional space for the

[a] State Key Laboratory of Rare Earth Resource Utilization, Changchun Institute of Applied Chemistry, Chinese Academy of Sciences, Changchun, Jilin 130022, China

[b] University of Chinese Academy of Sciences, Beijing 100049, China

*E-mail: xbzhang@ciac.ac.cn

uniform coating of EDTA-Fe-Na. As shown in the SEM images of Figure 2, obviously, EDTA-Fe-Na/GO inherits the nanosheet-like morphology of GO, and the enhanced surface roughness indicates the successful deposition of EDTA-Fe-Na on GO. And similar feature happens to EDTA-2Na/GO (Figure 2c). In addition, SEM element mapping images in Figure S1 prove the uniform dispersion of EDTA-Fe-Na on GO nanosheets. The phase evolution is then explored. XRD patterns (Figure 2d) reveal two reserved peaks for EDTA-Fe-Na/GO compared to EDTA-Fe-Na. In sharp contrast, no obvious peaks could be observed related to EDTA-2Na/GO coming from EDTA-2Na. The difference between them may be explained by the undestroyed strong Fe coordination species in the EDTA-Fe-Na molecules after dissolving, which is undoubtedly beneficial to the formation of Fe-N active sites in the following pyrolysis. The EDTA-Fe-Na/GO is converted into Fe-N-C catalyst (EFGC) by pyrolysis and subsequent acid etch. In this process, large amount of hierarchical porous structure is produced after removing the templates through thermal evaporation of Na and Fe particles being chemically etched, which leads to a high surface area with enhanced mass transfer efficiency.

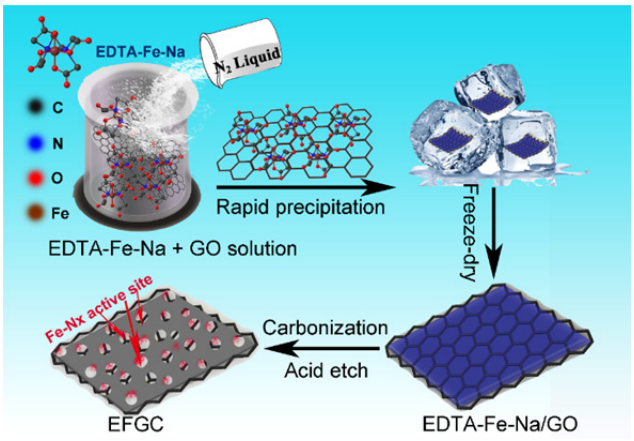

Figure 1 Schematic illustration of synthesis of the EFGC electrocatalyst.

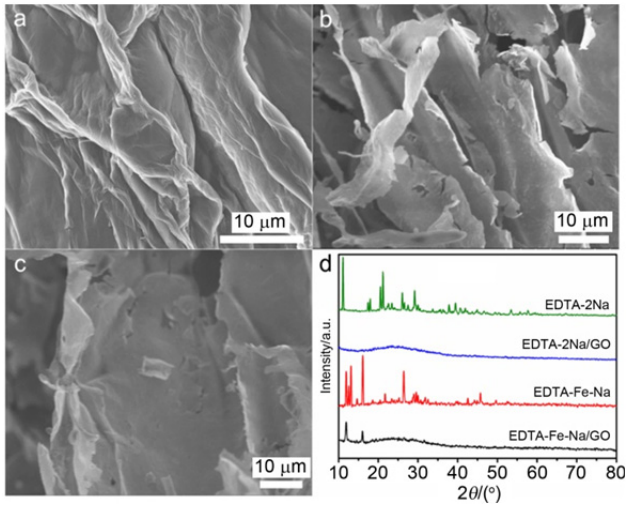

Figure 2 SEM images of (a) GO, (b) EDTA-Fe-Na/GO, and (c) EDTA-2Na/GO. (d) XRD patterns of EDTA-Fe-Na/GO, EDTA-2Na/GO, EDTA-Fe-Na, and EDTA-2Na.

The morphology and microstructure evolution of the as synthesized EFGC catalyst were then characterized. Obviously, when EDTA-Fe-Na/GO is converted into EFGC, the structural integrity of nanosheets is well preserved with further enhanced surface roughness (Figure 3a). Interestingly, the TEM image analysis (Figure 3b) reveals the more complicated microstructure, that is, the surface of the EFGC is composed of many multiple aperture pores. The larger pores belong to the etching of Fe particles, and the smaller pores should come from the evaporation and etching of Na. Three contrast samples of EFC, ENC, and ENGC are able to provide more relevant evidences. As displayed in Figure S2, diversity and differences are observed accordingly. EFC and ENC own blocky structure, the ENGC has a similar nanosheet-like morphology to EFGC (SEM images in Figure S2). More details provided in the TEM images reveal very different porous structures between any one. Wherein, the ENC and ENGC derived from EDTA-2Na and EDTA-2Na/GO without Fe have much abundant and even smaller pores, owing to the evaporation and etching of Na. In contrast, homogenous larger pores and even macropores appear in EFC, belonging to the etching of Fe particles, meanwhile, the smaller pores derived from Na still exist. This should explain the formation of hierarchical pore structures for EFGC. The porous feature and specific surface areas of EFGC were then further estimated by nitrogen adsorption-desorption isotherms. As displayed by the BET and BJH results in Figure 3c, EFGC has a BET surface area of 385 $m^2 \cdot g^{-1}$, slightly higher than that of EFC (363 $m^2 \cdot g^{-1}$); the pore volume is 1.22 $cm^3 \cdot g^{-1}$, slightly lower than that of EFC (1.41 $cm^3 \cdot g^{-1}$) as shown in Figure S3. Moreover, almost the same as expected, EFGC and EFC have similar pore size distribution, indicating the identical formation mechanism of pore structures between EFGC and EFC. The only slight difference should be attribute to the introduction of GO, which builds a three-dimensional channel and reduces the aggregation for increasing specific surface areas. A similar situation also happens to ENC and ENGC (Figures S4, 5), but the ENGC has much higher surface area and pore volume (541 $m^2 \cdot g^{-1}$ and 0.55 $cm^3 \cdot g^{-1}$) than ENC (249 $m^2 \cdot g^{-1}$ and 0.27 $cm^3 \cdot g^{-1}$). This phenomenon should be attributed to the lower accessibility of the smaller pores sealed in the interior of ENC, in contrast, the three-dimensional channel with extended nanosheets of ENGC promises greatly increased accessibility pores.

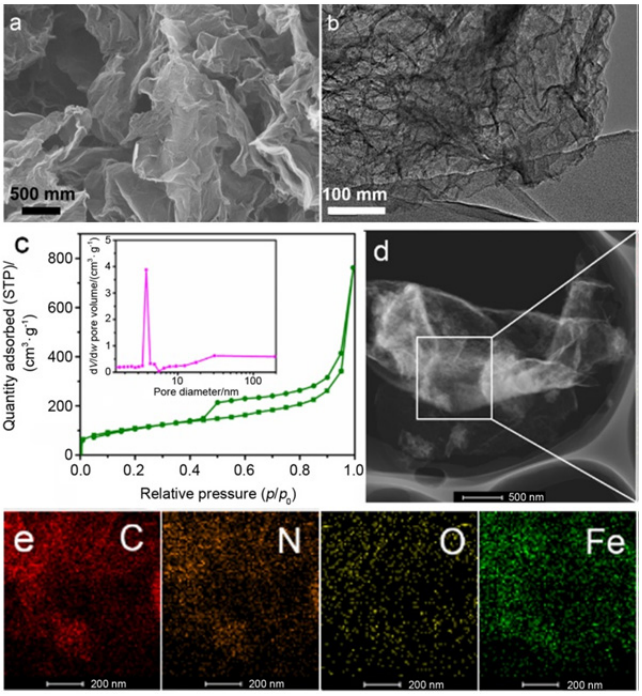

Figure 3 (a) SEM, (b) TEM images and (c) nitrogen adsorption-desorption isotherm (inset: pore size distribution) of EFGC. (d) HAADF-STEM image and (e) the corresponding C, N, O, and Fe elemental-mapping images of EFGC.

XRD patterns display two broad peaks at approximately 25°

and 44°, corresponding to carbon (002) and (101) diffractions (Figure S6). Compared to ENC and ENGC, EFGC and EFC have much lower degree of graphitization, meaning more defects and discontinuous carbon, which is generally caused by the heteroatom doping and too much porous structure. Raman spectra were then performed to analyze the defect level. Figure S7 reveals that EFGC has a high I_D/I_G ratio, implying the relatively high structural defects, which usually act as active sites and promote the catalytic performance. The element composition of four samples was analyzed with EDS to give the amount of heteroatom as shown in Table S1. It is observed that the N content of EFGC is determined to be 3.60%, slightly less than that of its counterparts (5.25% for EFC, and 11.30% for ENC). Much lower N content of ENGC (1.53%) should be induced by the thin layer distribution of EDTA-2Na on GO surface with less bulk density, which owns higher heating area and subsequently suffers from severe N loss during heat treatment. The coordination of Fe and N in EDTA-Fe-Na could help to anchor N atoms in pyrolysis process, thus resulting in more N doppping in EFGC than ENGC. However, Fe generally acts as catalysts promoting graphitization, and inevitably incurs a loss of N content, which are consistent with the contrast of N content between ENC (11.30%) and EFC (5.25%). The Fe content is 0.11% for EFGC and 0.04% for EFC. The higher content of Fe in EFGC compared to EFC should be due to highly uniform distribution of EDTA-Fe-Na on GO with low EDTA-Fe-Na powder packing, which could reduce the agglomeration of Fe particles, and thus can promote more Fe-Nx active sites during the pyrolysis process. Element mapping images of EFGC (Figure 3e) further suggest the homogeneous distribution of C, N, O, and Fe on porous nanosheets, as well as the ENGC (Figure S8). XPS was then performed on EFGC, EFC, ENGC, and ENC to investigate the difference of nitrogen chemical state between them. The N1s spectra of EFGC could be deconvoluted into two peaks, attributed to the pyridinic-N (398.2 eV) and graphitic-N (401 eV)[42-45] (Figure 4b). As shown in Figure 4c, EFGC and ENGC have higher ratio of pyridinic-N in the two nitrogen chemical states than EFC and ENC, which should be caused by the influence of GO and N doping in them during heat treatment. What's more, the pyridinic-N in both EFGC and EFC shows a positive shift compared to that of ENC and ENGC, which should arise from the coordination with Fe forming Fe-Nx active site, having been identified as one of the most effective active sites for ORR. FTIR spectra further prove the influence of this coordination, because the slight positive shift of the characteristic peaks of C=N (1600 cm^{-1}) shown in Figure S9 offers a new kind of proof. Generally, this coordination between N and Fe could be reflected in the Fe $2p_{3/2}$ XPS spectrum. As Figure 4d displayed, the peak at 709.4 eV is exactly attributed to the Fe-Nx coordination, the others stand for metallic Fe (707.1 eV), and different oxides (710.9 and 711.8 eV accompanied by satellite peaks at binding energy higher than 714 eV).[46,47]

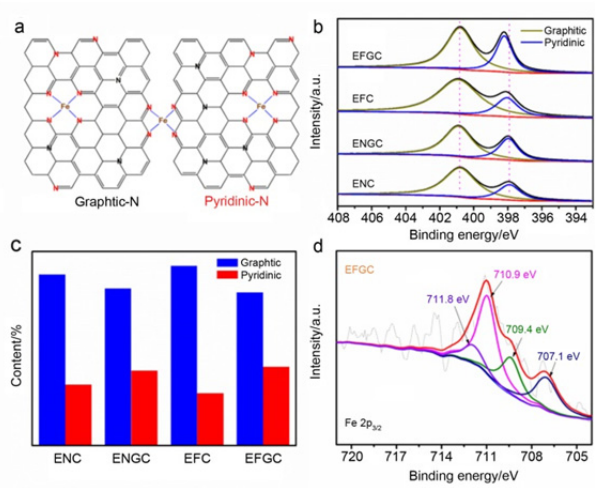

Figure 4 (a) Schematic representation of nitrogen chemical states. (b) N 1s XPS spectra of EFGC, EFC, ENGC, and ENC. (c) Relative ratios of the deconvoluted peak areas of the N 1s XPS spectra. (d) The Fe 2p XPS spectra of EFGC.

The electrocatalytic activity of catalysts was first evaluated by CV meansurments. No obvious redox peaks could be observed in N_2-saturated 0.1 mol/L KOH electrolyte for EFGC. However, upon changing to O_2, a clear cathodic peak arises at around 0.85 V (Figure 5a) immediately, which absolutely confirms the ORR electrocatalytic activity of EFGC. Same situation happens to the other three samples, but their cathodic peaks are much negative (Figure S10). RDE measurements were then further performed to get the polarization curves at the rotating speed of 1600 r/min (Figure 5b), in which, the EFGC catalyst reaches a more positive onset potential of 1.028 V and half-wave potential ($E_{1/2}$) of 0.86 V compared to those of Pt/C, which are 1.01 V (onset potential) and 0.85 V ($E_{1/2}$), respectively. In addition, larger limiting diffusion current density for EFGC is aslo existent. In contrast, the others (EFC, ENGC, and ENC) give much worse activities. The lower catalytic activity of EFC compared to EFGC could be atttributed to the introduction of graphene and higher Fe content for more active sites. In this case, graphene not only helps forming 3D space to make sure adequate mass transfer and more accessible exposed active sites for fast ionic specific conductivity, but also guarantees higher electronic conduction, thus reducing the polarization of ORR with improved onset potential and larger current density. The huge gap of catalytic activity between ENC and ENGC further comfirms the above verdict. The key role of Fe doping for superior ORR catalytic activity could be proven by the greatly improved onset potential of EFC (1.028 V) in comparison with that of ENGC (1.028 V). Structural advantage brought by graphene is reconfirmed according to the slighly higher limiting diffusion current density of ENGC (1 $mA \cdot cm^{-2}$). So that, the synergetic effect of highly active components, hierarchical porous structure, and large surface area should be responsible for superior ORR electrocatalytic activity. To the best of our knowledge, the ORR activity exhibited by EFGC is among the highest reported for carbon-based NPMCs (Table S2). In order to further evaluate the key role of Fe, SCN^- ion was chosen as a molecular probe to

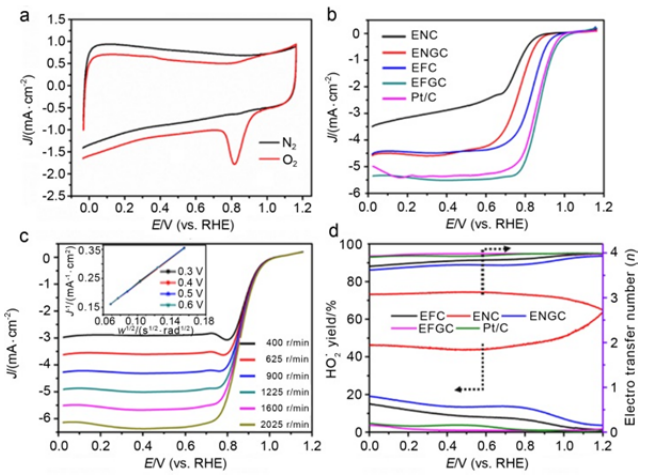

Figure 5 Electrochemical characterizations. (a) CVs of EFGC in N_2 and O_2-saturated 0.1 mol/L KOH at a scan rate of 50 $mV \cdot s^{-1}$. (b) RDE polarization plots of EFGC, EFC, ENGC, ENC, and commercial Pt/C catalysts at a scan rate of 10 $mV \cdot s^{-1}$ and rotation speed of 1600 r/min. (c) Voltammograms of EFGC at various speeds with a scan rate of 10 $mV \cdot s^{-1}$; inset is the corresponding K-L plots at different potentials. (d) Hydrogen peroxide yields and electron-transfer numbers.

poison Fe-N-C catalysts, due to its high affinity to Fe ions. Obviously, after treating with SCN^-, both the onset potential and $E_{1/2}$ of EFGC go through significant negative shift combined with decreased current density, which indicates that the Fe-Nx coordination compounds act as the real active sites for ORR. (Figure S12). According to earlier reports for classic Fe-N-C ORR catalysts,[48,49] the N ligand could modify the Fe ion's electronic structure to change d-electron density by relocating its redox potential, which could facilitate the direct adsorption of desolvated O_2 on Fe active centers, break of O═O bond and stabilizing the adsorbed intermediates, thus accelerating the progress of ORR.

RDE polarization plots at various rotation speeds of EFGC are then carried out and shown in Figure 5c. The Koutecky-Levich (K-L) equations at several potentials are further calculated to analyse the four-electron selectivity. The obvious linearity and parallelism of K-L plots for EFGC at various potentials shown in Figure 5c inset indicate that first-order reaction kinetics are related to the concentration of dissolved O_2. The electron transfer number (n) at the potential of 0.5 V is calculated to be 4.01, which is close to the theoretical value 4.0 of Pt/C, suggesting that the ORR process catalysed by EFGC most likely undergoes a route of direct four-electron. In comparison, the three contrasting samples undergo a low efficiency 2e pathway in varying degrees toward the formation of peroxide, the n values are 3.82, 3.70, and 2.7 for EFC, ENGC, and ENC respectively (Figure S13). For the purpose to study the selectivity toward 4e reduction by monitoring the formation of peroxide, an RRDE technique was carried out subsequently and the results are shown in Figure 5d. In the potential range from 0.2 to 0.8 V, the peroxide yield of EFGC is less than 3.5%, which is even better than that of Pt/C. The corresponding n values could be calculated from 3.95 to 3.98, alomst consistent with the above results based on K-L plots. When referring to EFC, ENC, and ENGC, the peroxide yield of any one is much higher, implying lower n values. Electrochemical stability is another important parameter, chronoamperometric measurements for EFGC and Pt/C were then conducted at a constant voltage of 0.55 V to evaluate and compare it (Figure 6a). After 20000 s of continuous electrolysis, the reduction current density of EFGC only decreases by about 2.8%. In sharp contrast, Pt/C suffers from serious loss of *ca*. 18.9%, indicating the superior durability of EFGC as a kind of ORR electrocatalyst. When it comes to the resistance to methanol crossover effect, EFGC shows greater advantage. Upon injection of methanol, a marked current decrease happens to Pt/C immediately, indicating the appearance of methanol oxidation reaction. As a contrast, the current change of EFGC is very slight and recovers quickly with almost negligible decrease, referring to great tolerance toward methanol crossover effect (Figure 6b).

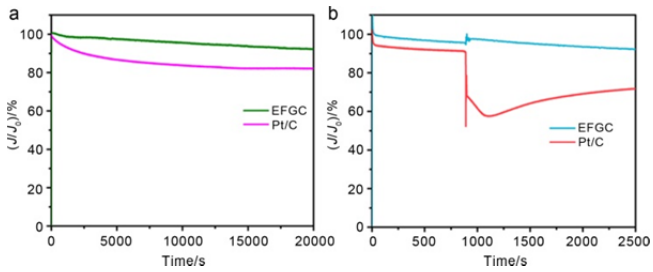

Figure 6 (a) Current-time chronoamperometric responses of EFGC and Pt/C at 0.55 V (at a rotation speed of 1600 r/min) over 20000 s. (b) Chronoamperometric responses of EFGC and Pt/C upon the addition of 2% (*V*/*V*) methanol after about 900 s.

In addition to alkaline medium, the electrocatalytic performance of EFGC towards ORR in acid medium (0.1 mol/L $HClO_4$) is also effective and competitive. As shown in Figure S15, the RDE polarization curves display an $E_{1/2}$ of 0.71 V for EFGC, which is just about a 59 mV negative shift compared with that of Pt/C, but much more positive than those of EFC (0.62 V), ENGC (0.55 V) and ENC (0.5 V). Although the activity of EFGC in acidic media is less than that under alkaline conditions, it is still one of the best recently reported carbon-based NPMCs in acid medium (Table S3). K-L plots reveal a 4e selectivity for ORR process of EFGC (Figure S16). SCN^- poison experiment proves the active site of Fe in acid medium (Figure S17). A much better stability is also realized for EFGC than Pt/C in acidic medium. After 20000 s continuous reduction, EFGC can reserve about 87.9% current density, in sharp contrast, Pt/C retains 75.2% (Figure S18a). Just like the alkaline envirenment, EFGC catalyst still retains great tolerance to methanol crossover effect (Figure S18b).

To assess the enormous potential in real applications, both AAEMFC and PEMFC were assembled with the EFGC and Pt/C cathodes for comparison. The performance of AEMFC is shown in Figure 7, thereof, the EFGC realizes an open circuit voltage (OCV) of 0.97 V and a peak power density of 330 $mW{\cdot}cm^{-2}$. Different from the results of three electrode tests, the commercial Pt/C gives a slightly higher performance than EFGC, involving an OPV of 1.05 V and a peak power density of 389 $mW{\cdot}cm^{-2}$. This phenomenon should be caused by the loose supporting structure of graphene in EFGC, which leads to a very thick catalytic layer on the MEA resulting in decreased mass transfer rate. As displayed in Figure S19a, much huge gap between EFGC and Pt/C appears in the PEMFC measurements, wherein, the peak power densities are 386 $mW{\cdot}cm^{-2}$ for EFGC and 945 $mW{\cdot}cm^{-2}$ for Pt/C. The PEMFCs for EFGC and Pt/C show higher performance, especially for Pt/C, higher MEA qualities and fast proton transfer may be responsible for that. Besides, the EFGC presents good one day and night stability both in AEMFC and PEMFC (Figures S19b, c). Considering the much cheap price, simple synthesis, expansion of production, and above acceptable results, EFGC can be successfully employed as a promising cathode catalyst in fuel cells.

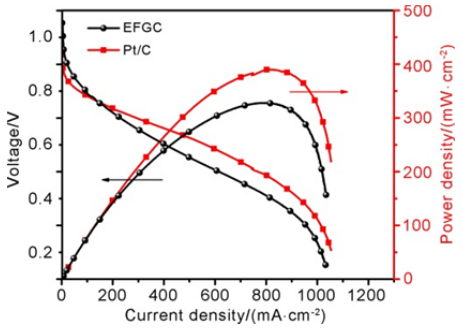

Figure 7 The cell voltage and power density of AEMFCs with EFGC and commercial Pt/C (40 wt%) as cathodes.

Conclusions

In summary, to take advantages of precursor-controlled synthesis in relation with the transition metal coordination complex for highly active ORR electrocatalyst, a cheap EDTA-Fe-Na chelate was anchored on graphene to construct the homogeneous precursor composite through rapid nucleation and deposition process assisted by liquid nitrogen to develop Fe-N-C ORR electrocatalysts. On the basis of the inherent nature of EDTA-Fe-Na and graphene, the uncontrolled agglomeration and microstructural inhomogeneity of derived Fe-N-C catalysts during pyrolysis can be prevented to the maximum extent. Benefiting from abundant Fe-Nx active species, 2D conterminous conductive networks and mass transfer channels, the EFGC presents advantageous catalytic properties for ORR in alkaline media, including high activity with more positive onset and half-wave potential, efficient 4e selec-

tivity, a long-term stability, and anti-poisoning power, all of which are superior to those of commercial Pt/C. Especially, both the assembled alkaline and acid fuel cells based on the EFGC cathode catalysts reveal excellent performance with high open-circuit voltage and power density. The developed synthesis strategy opens new avenues for other carbon-based material synthesis systems for broad applications including supercapacitors, batteries, and other new energy devices.

Experimental

Preparation of materials. All reagents were of analytical grade and used without further purification. To obtain the uniform precursor of a mixture of iron-EDTA complex (EDTA-Fe-Na) and GO (EDTA-Fe-Na/GO), 1 g EDTA-Fe-Na was dissolved into 10 mL deionized water and dropped into 10 mL GO suspension (6 mg·mL^{-1}) under stirring. 1 h later, the stable and finely-dispersed mixture was rapidly frozen in liquid nitrogen and further dried by freeze drying. For the synthesis of Fe-N-C catalysts, EDTA-Fe-Na/GO was first calcined under flow N_2 at 400 °C for 1 h, then etched with 1 mol/L HCl and washed with deionized water and ethanol several times. Subsequently, the second heat treatment was carried out at 950 °C for 2 h in N_2 as well as the etching. The final catalyst (named EFGC) was got after a third calcination at 950 °C for 1 h in N_2. For comparison, we prepared three other samples with different precursor components under the same conditions (EDTA-2Na/GO for ENGC, EDTA-Fe-Na for EFC, and EDTA-2Na for ENC).

Physical characterizations. Powder X-ray diffraction (XRD) measurement was performed using an X-ray diffractometer (micro-XRD, Rigaku, Japan) with Cu Kα (λ=0.15406 nm). Scanning electron microscopy (SEM) and elemental-mapping were carried out with a field emission scanning electron microanalyzer (Hitachi S4800) operating at an accelerating voltage of 10 kV. Transmission electron microscope (TEM), energy dispersive X-ray spectroscopy (EDS), and elemental-mapping were performed on a FEI Tecnai G2 S-Twin instrument with a field emission gun operating at 200 kV. Nitrogen adsorption-desorption measurements were performed on a Micromeritics ASAP 2020 adsorption analyser. Specific surface areas and pore characteristics were analyzed by the Brunaure-Emmert-Teller (BET) and Barrett-Joyner-Halenda (BJH) method, respectively. Fourier transform infrared (FT-IR) spectra were analyzed on a Nicolet iS5 spectrometer. Raman spectra were collected with a micro-Raman spectrometer (Renishaw) with a laser of 532 nm wavelength. X-ray photoelectron spectroscopy (XPS) was analyzed on a VG Scientific ESCALAB MKII X-ray photoelectron spectrometer using an Al Kα source. All the electrochemical measurements were performed using a BioLogic VMP3 electrochemical workstation at room temperature.

Electrochemical measurements. A three-electrode system was adopted in all electrochemical measurements at room temperature, in which, Pt sheet and Ag/AgCl in saturated KCl were exploited as counter and reference electrodes, respectively. A glassy carbon (GC) rotating ring-disk electrode (RRDE) (5.61 mm in diameter) coated with smooth and wrinkle-free catalyst was served as work electrode. In order to achieve a fine work electrode, firstly, blend 5 mg catalyst and 50 μL of 5 wt% Nafion ethanol solution into 1 mL ethanol under sonication for 0.5 h to prepare catalyst ink. Secondly, drop 10 μL catalyst ink on the surface of the GC disk electrode to yield a catalyst loading of 0.2 mg·cm^{-2}. For comparison, all samples including the commercial Pt/C catalyst (nominally 20 wt% on carbon black from Johnson Matthey) were applied to GC electrode by the same procedure.

Cyclic voltammetry (CV) was conducted in N_2 or O_2-saturated 0.1 mol/L KOH in the potential range of –1.0 V and 0.2 V (versus Ag/AgCl) at a scan rate of 50 mV·s^{-1}. All the measured potentials versus Ag/AgCl were converted to a reversible hydrogen electrode (RHE) scale according to the Nernst equation ($E_{RHE}=E_{Ag/AgCl}+0.059pH+0.197$). The ORR RDE polarization measurements were performed at different rotating speeds from 400 to 2025 r/min at a sweep rate of 10 mV·s^{-1}. The number of transferred electrons was calculated according to the Koutecky-Levich equation:

$$1/j=1/j_d+1/j_k=1/(B\omega^{1/2})+1/j_k \quad (1)$$

$$B=0.62nFC_O D_O^{2/3} v^{-1/6} \quad (2)$$

where j (mA·cm^{-2}) is the measured current density, which is related to the diffusion-limiting current (j_d) and the kinetic current (j_k), F is the Faraday constant (96485 C·mol^{-1}), D_O is the diffusion coefficient of O_2 in 0.1 mol·L^{-1} KOH (1.9×10^{-5} cm^2·s^{-1}), v is the kinematic viscosity of water (0.01 cm^2·s^{-1}), C_O is the bulk concentration of O_2 in O_2-saturated 0.1 mol·L^{-1} KOH (1.2×10^{-6} mol·cm^{-3}), ω is the RDE rotation rate, and n is the electron transfer number.

RRDE system was further carreid out to detect peroxide species formed at the disc electrode, wherein, the potential on the Pt ring was set to 0.5 V (*vs* Ag/AgCl).

The peroxide species yield and four-electron selectivity (electron transfer number: n) of catalysts were calculated from the following equations, respectively:

$$H_2O_2(\%)=200(I_R/N)/(I_R/N+I_D) \quad (3)$$

$$n=4I_D/(I_R/N+I_D) \quad (4)$$

Here, I_D and I_R are the disk and ring currents, respectively, and N =0.37 is the ring collection efficiency.

Membrane electrode assembly (MEAs) preparation and fuel cell tests. 40 wt% Pt/C (Johnson Matthey) and EFGC served as anode and cathode catalysts, respectively. For the proton-exchange membrane fuel cell (PEMFC), the Pt/C catalyst ink was sprayed onto the DuPont 112 Nafion membrane to deposit a catalyst layer with a Pt loading of 0.3 mg·cm^{-2} as the anode and the EFGC loading of 4 mg·cm^{-2} as the cathode on the other side (the ratio of catalyst to Nafion was 3 : 1). Two pieces of hydrophobic carbon papers (Toray TGP-H-090) and the membrane (coated with catalysts on both sides) were sandwiched together and pressed at 3 MPa for 2 min at 130 °C to prepare a MEA. The MEA was then assembled in a H_2/O_2 fuel cell with an active area of 1 cm^2. Pure H_2 and O_2 were supplied as fuel and oxidant with a flow rate of 300 and 200 sccm, respectively. The operating condition was set to 80 °C and 100% RH. Polarization curves and power density were obtained using the *I-V* technique in electrochemical workstation with a scan rate of 5 mV·s^{-1}.

For the alkaline anionic membrane fuel cell (AAEMFC), the aQAPS-S_8 membrane and 2 wt% aQAPS-S_{14} ionomer solution (Hephas Energy Co., Ltd.) were used. Before using, the aQAPS-S_8 membrane (in chloride form) was first immersed in 1 mol/L KOH for 1 d to exchange OH^- and then stored in deionized water. The catalyst loading was the same as that for PEMFC, but, the MEA was pressed at 3 MPa for 2 min at 80 °C. The test conditions were identical to that for PEMFC. For comparison, 40 % Pt/C with a Pt loading of 0.3 mg·cm^{-2} was also used as cathode both in PEMFC and AAEMFC.

Supporting Information

The supporting information for this article is available on the WWW under https://doi.org/10.1002/cjoc.201700752.

Acknowledgement

This work was financially supported by Ministry of Science and Technology of China (Nos. 2016YFB0100103 and 2017YFA0206704), National Program on Key Basic Research Project of China (No. 2014CB932300), Strategic Priority Research Program of the Chinese Academy of Sciences (No. XDA09010404), Technology and Industry for National Defense of China (No. JCKY2016130B010), and

National Natural Science Foundation of China (Nos. 51771177, 21422108 and 51472232).

References

[1] Zhou, M.; Wang, H. L.; Guo, S. *Chem. Soc. Rev.* **2016**, *45*, 1273.

[2] (a) Shao, M.; Chang, Q.; Dodelet, J. P.; Chenitz, R. *Chem. Rev.* **2016**, *116*, 3594; (b) Cao, J.; Zhu, Z.; Zhao, W. *Chin. J. Chem.* **2016**, *34*, 1086; (c) Xu, X.; Peng, S.; Zhang, J.; Lu, S.; Xiang, Y. *Acta Chim. Sinica* **2016**, *74*, 271.

[3] (a) Li, J.; Zhang, X.; Pan, B.; Xu, J.; Liu, L.; Ma, J.; Yang, M.; Zhang, Z.; Tong, Z. *Chin. J. Chem.* **2016**, *34*, 1021; (b) Li, Q.; Xu, H.; Tong, Y. *Acta Chim. Sinica* **2017**, *75*, 193; (c) Li, N. *Chin. J. Chem.* **2016**, *34*, 1129.

[4] Seh, Z. W.; Kibsgaard, J.; Dickens, C. F.; Chorkendorff, I.; Norskov, J. K.; Jaramillo, T. F. *Science* **2017**, *355*, 146.

[5] Zhong, H. X.; Wang, J.; Zhang, Y. W.; Xu, W. L.; Xing, W.; Xu, D.; Zhang, Y. F.; Zhang, X. B. *Angew. Chem. Int. Ed.* **2014**, *53*, 14235.

[6] Ye, L.; Chai, G.; Wen, Z. *Adv. Funct. Mater.* **2017**, *27*, 1606190.

[7] Xia, B. Y.; Yan, Y.; Li, N.; Wu, H. B.; Lou, X. W.; Wang, X. *Nat. Energy* **2016**, *1*, 15006.

[8] Tian, G. L.; Zhao, M. Q.; Yu, D.; Kong, X. Y.; Huang, J. Q.; Zhang, Q.; Wei, F. *Small* **2014**, *10*, 2251.

[9] (a) Zhao, X.; Chen, S.; Fang, Z.; Ding, J.; Sang, W.; Wang, Y.; Zhao, J.; Peng, Z.; Zeng, J. *J. Am. Chem. Soc.* **2015**, *137*, 2804; (b) Tao, X.; Li, L.; Qi, X.; Wei, Z. *Acta Chim. Sinica* **2017**, *75*, 237; (c) Wang, S.; He, P.; He, M. *Chin. J. Chem.* **2018**, *36*, 37.

[10] (a) Zhang, S.; Hao, Y.; Su, D.; Doan-Nguyen, V. V.; Wu, Y.; Li, J.; Sun, S.; Murray, C. B. *J. Am. Chem. Soc.* **2014**, *136*, 15921; (b) Li, D.; Zhang, Z.; Zang, P.; Ma, Y.; Wu, Q.; Yang, L.; Chen, Q.; Wang, X.; Hu, Z. *Acta Chim. Sinica* **2016**, *74*, 587.

[11] Su, C.-Y.; Cheng, H.; Li, W.; Liu, Z.-Q.; Li, N.; Hou, Z.; Bai, F.-Q.; Zhang, H.-X.; Ma, T.-Y. *Adv. Energy Mater.* **2017**, *7*, 1602420.

[12] Lu, Y.; Jiang, Y.; Gao, X.; Wang, X.; Chen, W. *J. Am. Chem. Soc.* **2014**, *136*, 11687.

[13] Cheng, F.; Zhang, T.; Zhang, Y.; Du, J.; Han, X.; Chen, J. *Angew. Chem. Int. Ed.* **2013**, *52*, 2474.

[14] Chen, W.; Sin, M.; Wei, P.-J.; Zhang, Q.-L.; Liu, J.-G. *Chin. J. Chem.* **2016**, *34*, 878.

[15] Zuo, L.; Jiang, L.; Zhu, J.-J. *Chin. J. Chem.* **2017**, *35*, 969.

[16] Gao, S.; Chen, Y.; Fan, H.; Wei, X.; Hu, C.; Luo, H.; Qu, L. *J. Mater. Chem. A* **2014**, *2*, 3317.

[17] Sha, H.-D.; Yuan, X.; Li, L.; Ma, Z.; Ma, Z.-F.; Zhang, L.; Zhang, J. *J. Power Sources* **2014**, *255*, 76.

[18] Yang, H. B.; Miao, J.; Hung, S. F.; Chen, J.; Tao, H. B.; Wang, X.; Zhang, L.; Chen, R.; Gao, J.; Chen, H. M.; Dai, L.; Liu, B. *Sci. Adv.* **2016**, *2*, e1501122.

[19] Wang, S.; Zhang, L.; Xia, Z.; Roy, A.; Chang, D. W.; Baek, J. B.; Dai, L. *Angew. Chem. Int. Ed.* **2012**, *51*, 4209.

[20] Cheon, J. Y.; Kim, J. H.; Goddeti, K. C.; Park, J. Y.; Joo, S. H. *J. Am. Chem. Soc.* **2014**, *136*, 8875.

[21] Chang, Y.; Hong, F.; He, C.; Zhang, Q.; Liu, J. *Adv. Mater.* **2013**, *25*, 4794.

[22] You, C.; Liao, S.; Li, H.; Hou, S.; Peng, H.; Zeng, X.; Liu, F.; Zheng, R.; Fu, Z.; Li, Y. *Carbon* **2014**, *69*, 294.

[23] Zhou, X.; Yang, Z.; Nie, H.; Yao, Z.; Zhang, L.; Huang, S. *J. Power Sources* **2011**, *196*, 9970.

[24] Kuttiyiel, K. A.; Sasaki, K.; Park, G.-G.; Vukmirovic, M. B.; Wu, L.; Zhu, Y.; Chen, J. G.; Adzic, R. R. *Chem. Commun.* **2017**, *53*, 1660.

[25] Cui, X.; Yang, S.; Yan, X.; Leng, J.; Shuang, S.; Ajayan, P. M.; Zhang, Z. *Adv. Funct. Mater.* **2016**, *26*, 5708.

[26] Wu, G.; More, K. L.; Johnston, C. M.; Zelenay, P. *Science* **2011**, *332*, 443.

[27] Wang, X.; Zhang, H.; Lin, H.; Gupta, S.; Wang, C.; Tao, Z.; Fu, H.; Wang, T.; Zheng, J.; Wu, G. *Nano Energy* **2016**, *25*, 110.

[28] Gokhale, R.; Chen, Y.; Serov, A.; Artyushkova, K.; Atanassov, P. *Electrochim. Acta* **2017**, *224*, 49.

[29] Ferrero, G. A.; Preuss, K.; Marinovic, A.; Jorge, A. B.; Mansor, N.; Brett, D. J.; Fuertes, A. B.; Sevilla, M.; Titirici, M.-M. *ACS Nano* **2016**, *10*, 5922.

[30] Kramm, U. I.; Geppert, I. H.; Behrends, J.; Lips, K.; Fiechter, S.; Bogdanoff, P. *J. Am. Chem. Soc.* **2016**, *138*, 635.

[31] Ding, W.; Li, L.; Xiong, K.; Wang, Y.; Li, W.; Nie, Y.; Chen, S.; Qi, X.; Wei, Z. *J. Am. Chem. Soc.* **2015**, *137*, 5414.

[32] (a) Zhong, G.; Wang, H.; Yu, H.; Peng, F. *Acta Chim. Sinica* **2017**, *75*, 943; (b) Chen, X.; Yan, H.; Xia, D. *Acta Chim. Sinica* **2017**, *75*, 189.

[33] Mao, S.; Wen, Z.; Huang, T.; Hou, Y.; Chen, J. *Energy Environ. Sci.* **2014**, *7*, 609.

[34] Liang, Y.; Li, Y.; Wang, H.; Dai, H. *J. Am. Chem. Soc.* **2013**, *135*, 8452.

[35] (a) Fan, X.; Yang, Z.; Liu, Z. *Chin. J. Chem.* **2016**, *34*, 107; (b) Song, C.; Sun, X.; Ye, K.; Cheng, K.; Yan, J.; Cao, D. *Acta Chim. Sinica* **2017**, *75*, 1003.

[36] Shao, Y. Y.; Sui, J. H.; Yin, G. P.; Gao, Y. Z. *Appl. Catal. B* **2008**, *79*, 89.

[37] Li, X. H.; Antonietti, M. *Angew. Chem. Int. Ed.* **2013**, *52*, 4572.

[38] Wu, Z. S.; Chen, L.; Liu, J.; Parvez, K.; Liang, H.; Shu, J.; Sachdev, H.; Graf, R.; Feng, X.; Mullen, K. *Adv. Mater.* **2014**, *26*, 1450.

[39] Lin, Q.; Bu, X.; Kong, A.; Mao, C.; Bu, F.; Feng, P. *Adv. Mater.* **2015**, *27*, 3431.

[40] Chang, S. T.; Wang, C.-H.; Du, H.-Y.; Hsu, H.-C.; Kang, C.-M.; Chen, C.-C.; Wu, J. C. S.; Yen, S.-C.; Huang, W.-F.; Chen, L.-C.; Lin, M. C.; Chen, K.-H. *Energy Environ. Sci.* **2012**, *5*, 5305.

[41] Deville, S.; Saiz, E.; Nalla, R. K.; Tomsia, A. P. *Science* **2006**, *311*, 515.

[42] Yang, D. S.; Bhattacharjya, D.; Inamdar, S.; Park, J.; Yu, J. S. *J. Am. Chem. Soc.* **2012**, *134*, 16127.

[43] Chen, S.; Wei, Z.; Qi, X.; Dong, L.; Guo, Y. G.; Wan, L.; Shao, Z.; Li, L. *J. Am. Chem. Soc.* **2012**, *134*, 13252.

[44] Liang, Y.; Li, Y.; Wang, H.; Zhou, J.; Wang, J.; Regier, T.; Dai, H. *Nat. Mater.* **2011**, *10*, 780.

[45] Li, Y.; Zhou, W.; Wang, H.; Xie, L.; Liang, Y.; Wei, F.; Idrobo, J. C.; Pennycook, S. J.; Dai, H. *Nat. Nanotechnol.* **2012**, *7*, 394.

[46] Liu, J.; Sun, X. J.; Song, P.; Zhang, Y. W.; Xing, W.; Xu, W. L. *Adv. Mater.* **2013**, *25*, 6879.

[47] Wang, L.; Yin, J.; Zhao, L.; Tian, C. G.; Yu, P.; Wang, J. Q.; Fu, H. G. *Chem. Commun.* **2013**, *49*, 3022.

[48] Ramaswamy, N.; Tylus, U.; Jia, Q.; Mukerjee, S. *J. Am. Chem. Soc.* **2013**, *135*, 15443.

[49] Zitolo, A.; Goellner, V.; Armel, V.; Sougrati, M. T.; Mineva, T.; Stievano, L.; Fonda, E.; Jaouen, F. *Nat. Mater.* **2015**, *14*, 937.

Manuscript received: December 7, 2017
Manuscript revised: January 20, 2018
Manuscript accepted: January 24, 2018
Accepted manuscript online: January 26, 2018
Version of record online: XXXX, 2018

